A numerical and scaled experimental study on ride comfort enhancement of a high-speed rail vehicle through optimizing traction rod stiffness

Vahid Bokaeian[1], Mohammad Ali Rezvani[1*] and Robert Arcos[2]

[1]Center of Excellence in Railway Transportation, School of Railway Engineering, Iran University of Science and Technology, Tehran, Iran.
[2]Serra Húnter fellow, Acoustical and Mechanical Engineering Laboratory, Universitat Politècnica de Catalunya, Terrassa, Spain

Abstract

In this research, the effect of rail vehicle carbody's flexural modes on the ride comfort of an example high-speed railway vehicle is investigated. The vehicle is modeled as a rigid multi-body system, where the rigid body vertical, longitudinal, pitch, and roll degrees of freedom of the carbody and bogie frames and the rigid body vertical and roll degrees of freedom of the wheelsets are considered. An Euler-Bernoulli beam theory is used to account for the flexural motion of the carbody. The longitudinal interaction between carbody and bogie through the traction rod is modeled as a nonlinear spring element. The corresponding equations of motion of the system in the frequency-domain are obtained by using the equivalent linearization method. The effect of the traction rod is explored by using this model. Also, the optimal stiffness of the traction rod element that minimizes the flexural vibrations of the carbody is obtained through a genetic algorithm. With the optimal stiffness for the traction rod, the ride quality index at the center of the carbody floor is improved by 41 percent at a speed of 300 km/h. For the validation of numerical results, a scaled model of the vehicle with a scale factor of 24.5 was constructed and its associated results are presented. The model was excited by random input signals, which were generated based on the power spectral density of the track irregularity function. The agreement between the simulation results and the scaled experimental outcome when compared with the measured data from other sources is found to be satisfactory. In the framework of the physical scaled model, the filtering effect due to the vehicle bogie base is also examined.

Keywords: railway vehicle dynamics; ride comfort; nonlinear dynamic interaction; random vibration; frequency-domain analysis.

1 Introduction

To increase the speed of travel, it is a common practice to use lighter materials for the construction of railway vehicles. Among other benefits, it is also beneficial in the mitigation of noise emissions and ground-borne vibrations. In contrast, reducing the mass of the carbody can adversely affect its ride comfort. Indeed, natural frequencies of flexural modes of carbody decrease by reduction of its weight and can interfere with passenger comfort (Zhou et al., 2009).

Several studies have focused on the effect of the carbody's flexural modes on the ride quality index of railway vehicles. Carlbom (2000), Zhou et al. (2009), Younesian et al. (2014), Shi and Wu (2016), Ling et al. (2018), Akiyama et al. (2019), and Bokaeian et al. (2019) studied the effect of flexural modes of the carbody on passengers' ride comfort. Those researches demonstrated the significant influence of the first bending mode of the carbody on its ride quality.

There exist some passive solutions for improving the ride quality of vehicles, such as the use of dynamic vibration absorbers (DVAs). Tomioka and Takigami (2010), Gong et al. (2012), Sun et al. (2017), Huang et al. (2018), Wang et al. (2018), and Gong et al. (2019)

implemented various passive solutions to enhance the passenger's ride comfort of railway vehicles. In contrast to the passive methods, there are also active methods to eliminate flexural vibrations of carbody. These include the use of control mechanisms on the primary and the secondary suspension systems and the use of smart piezoelectric materials. Schandl et al. (2007), Sugahara et al. (2009), Kamada et al. (2010), Sun et al. (2016), Ripamonti and Chiarabaglio (2019), and Wen et al. (2019) improved ride quality of railway vehicles by the application of active methods.

The prime purpose of the present research is the reduction of vibration associated with the first bending mode of an example high-speed railway vehicle carbody. This is performed by taking advantage of the bogie-carbody dynamic interaction. Such an idea was initially proposed by Tomioka and Takigami (2010), who suggested using the vehicle bogies as DVAs acting on the carbody.

However, in the research by Tomioka and Takigami (2010), traction rod stiffness was considered to be a linear spring element, while in the present research, a nonlinear performance for this component is demonstrated and adopted. Such nonlinear behavior of the traction rod is based on experimental measurements that are performed in the framework of this research.

It is known that there is a coupled mode between the bogie pitch and the bending deformation of the carbody. In the present research, a more complex coupling phenomenon is considered. Besides the first bending mode, the first twisting and the second bending modes of the carbody, together with the rigid roll and the pitching of the bogie frames, are also included in the dynamic model of the vehicle. The ride quality calculations are based on the EN12299:2009 standard.

2 Derivation of the dynamic model

The dynamic model of the vehicle is based on a combination of its rigid and flexible modes. The example model is the Shinkansen (series 100) high-speed rail vehicle. The degrees of freedom considered for the rigid motion of carbody and bogie frames are the vertical and longitudinal translations and the pitch and roll rotations. The degrees of freedom for the wheelsets include bounce and roll. Flexural modes of carbody include both bending and twisting.

The wheel-rail normal contacts are modeled by assuming the equivalent linear spring model, which is obtained by using the Hertzian contact theory. It is also assumed that the wheelsets do not vibrate in the longitudinal direction. Therefore, the wheel-rail longitudinal contact forces are not included. The vehicle is excited by vertical track irregularity that is of a random nature. The frequency-domain analysis is used. The time-domain nonlinear equations of motions of the vehicle are transformed into the frequency-domain using the equivalent linearization method (Roberts and Spanos, 2003). A genetic algorithm is used to minimize the effect of the first bending mode of carbody on its ride quality, utilizing optimization of traction rod stiffness.

In the framework of this modeling scheme, the effect of the bogie-carbody dynamic interaction on the vehicle bounce is intensely investigated, and the optimal stiffness of the traction rod is evaluated. For experimental validation of results, a scaled model of the selected vehicle at the scale of 1:24.5 is built.

2.1 Modeling the bogie-carbody dynamic interaction

Figure 1 presents the proposed model of the example vehicle. Figure 1(c) illustrates a schematic of the vehicle while its carbody deforms under the influence of its first bending

mode. The bogie-carbody dynamic interaction in the longitudinal direction which arises from carbody's bending deformation is considered via the traction rod elements and the yaw dampers.

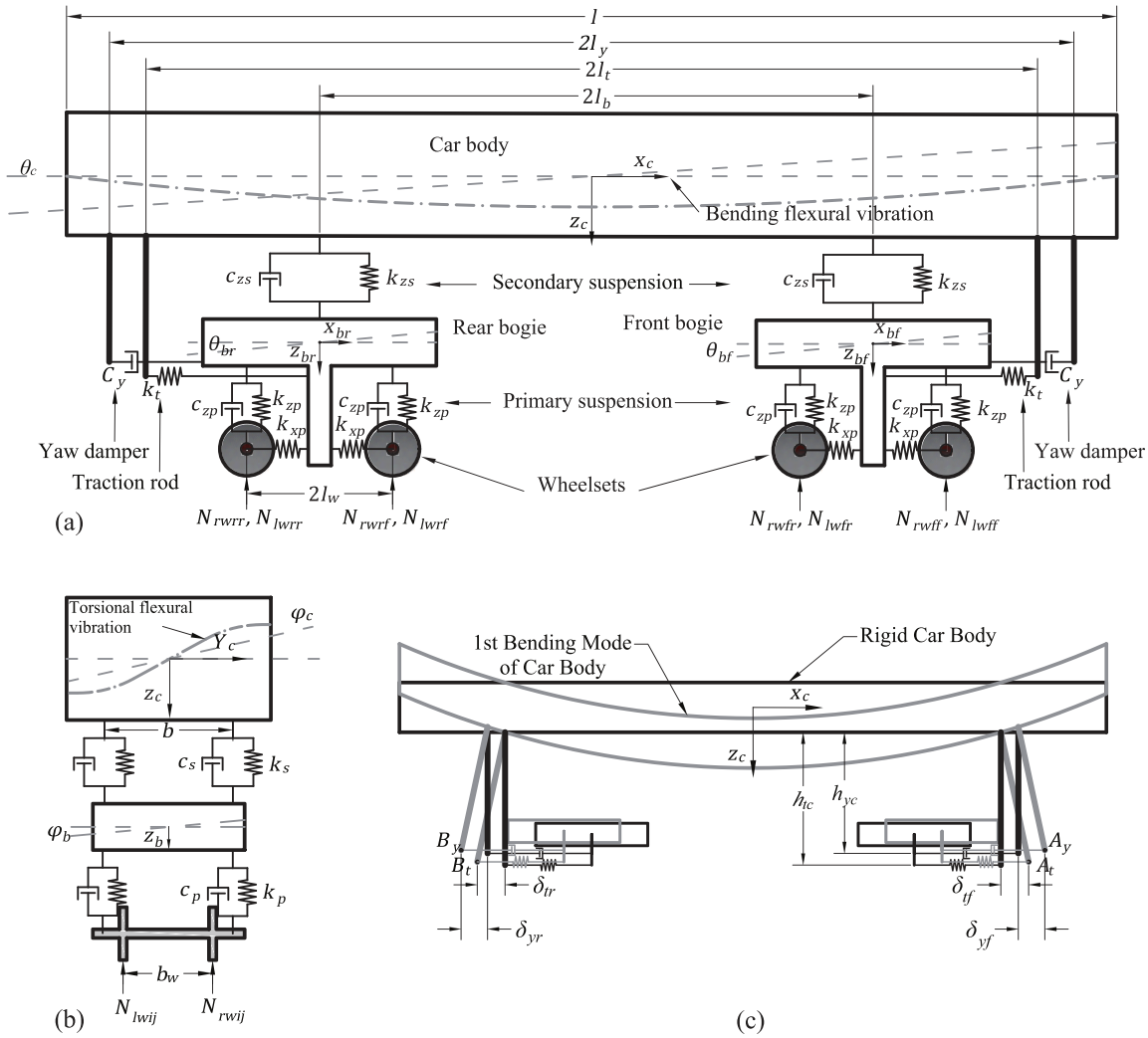

Figure 1. The proposed analytical model of a Shinkansen (Series 100) high-speed railway vehicle; a) longitudinal view, b) transversal view, c) schematic of the deformed carbody.

Due to the bending deformation, the connecting points of the carbody to the traction rods and yaw dampers (points A_i and B_i in Figure 1(c)) move in the longitudinal direction to the amounts of $\delta_{if} = z_c^{fb'}(l_{if}, t)h_{ic} + \theta_c h_{ic}$ and $\delta_{ir} = z_c^{fb'}(l_{ir}, t)h_{ic} + \theta_c h_{ic}$, respectively, where $z_c^{fb}(x, t)$ is the bending deformation of the carbody, and l_{tf} and l_{tr} are defined in Table A-1. Sub-index i needs to be replaced by t or y to represent the longitudinal displacement of the traction rod or the yaw damper connection points, respectively. The symbol ($'$) is for the derivative with respect to the displacement in the longitudinal direction. Figure 2 illustrates the longitudinal and vertical motions of the connection points between the front bogie and carbody through the traction rod and yaw damper.

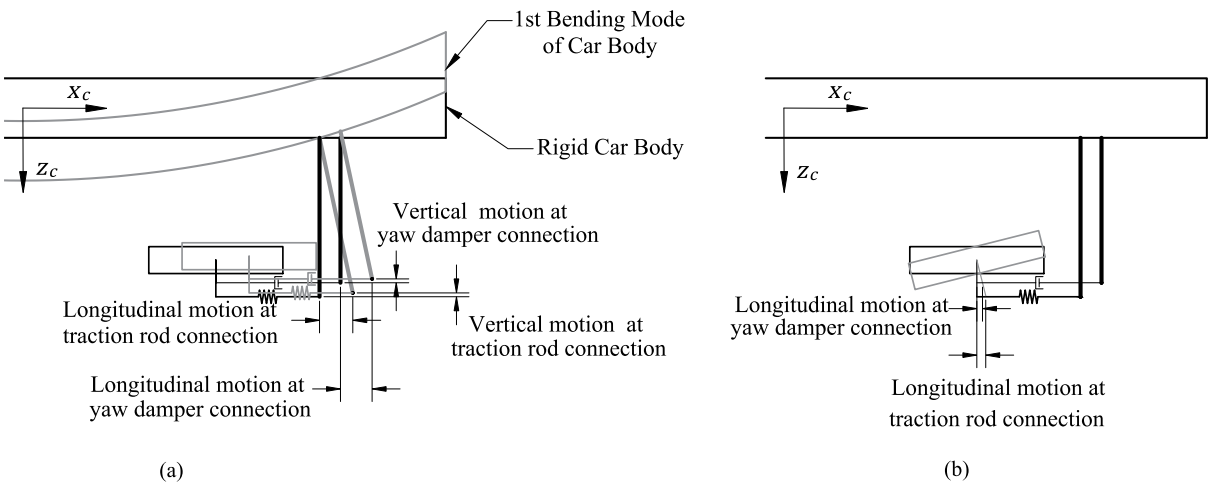

Figure 2. Vertical and longitudinal motions at traction rod and yaw damper connection points due to a) vertical motion of bogie frame and bending deformation of carbody and due to b) pitching of bogie frame.

The bogie-carbody dynamic interaction can be induced by three types of motions. These include the vertical and longitudinal motions of the bogie-carbody connection point due to the bending deformation of the carbody, and the longitudinal motion of the bogie-carbody connection point corresponding to the pitching of the bogie frames. Based on the geometrical observations that are presented in Figure 2, the most significant motion is related to the longitudinal displacements of the connection points due to the bending deformation of the carbody and pitching of the bogie frame.

The equations of motion in the longitudinal direction of the vehicle with the assumption of fixed wheelsets are;

$$m_c \ddot{x}_c = -f_{tf} - f_{tr} - f_{yf} - f_{yr} \tag{1}$$

$$m_{bf} \ddot{x}_{bf} = f_{tf} + f_{yf} - 2k_{xp} x_{bf} \tag{2}$$

$$m_{br} \ddot{x}_{br} = f_{tr} + f_{yr} - 2k_{px} x_{br} \tag{3}$$

where, m_c and m_b are masses of the carbody and bogie frame, respectively. f_{ti} and f_{yi} represent the longitudinal forces related to the traction rod and the yaw damper, respectively. Figure 3(a) presents the traction rod element for the selected vehicle. This element consists of two rubber bushes at the ends of a rigid rod. Figure 3(b) presents the mechanical model for this element, where k_{R1} and k_{R2} are the stiffness's of the two bushes on the two ends of this rod. With the assumption of same stiffness for both bushes, the equivalent stiffness of this rod in the longitudinal direction is

$$k_t = \frac{k_R}{2} \tag{4}$$

where $k_R = k_{R1} = k_{R2}$.

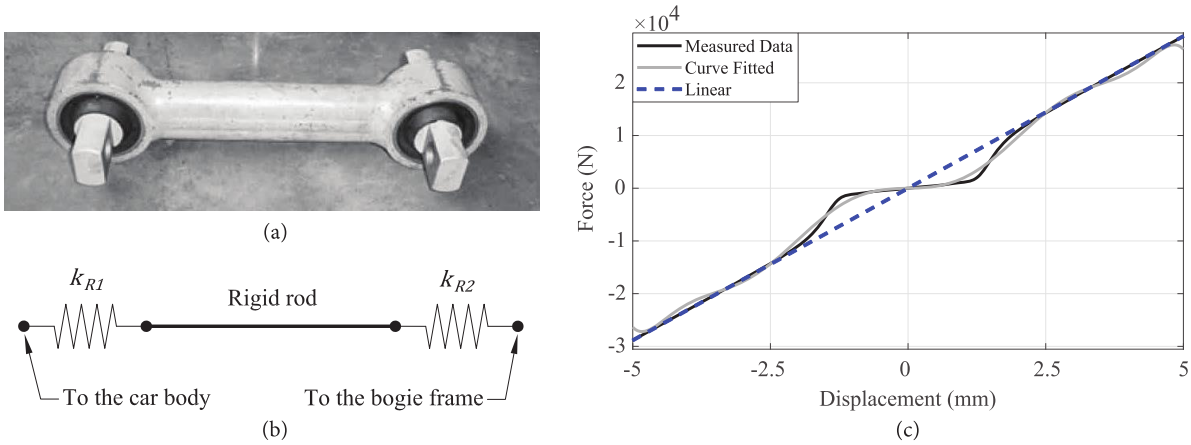

Figure 3. Traction rod element. a) The Shinkansen train traction rod (Tomioka and Takigami, 2010), b) Mechanical model of traction rod element, c) Dynamic behavior of traction rod element.

Figure 3(c) presents two models for the stiffness of the traction rod element. The first model, proposed by Tomioka and Takigami (2010), considers the traction rod stiffness as linear. The second is a nonlinear model based on the experimentally measured data that were obtained during the present research. As a result, stiffness of traction rod is considered a nonlinear function of its deformation, as presented in Equation (5).

$$k_{tNL}(\delta) = 2k_9\delta^8 + 2k_8\delta^6|\delta| + 2k_7\delta^6 + 2k_6\delta^4|\delta| + 2k_5\delta^4 + 2k_4\delta^2|\delta| + 2k_3\delta^2 + 2k_2\delta + 2k_1, \tag{5}$$

The k_i coefficients that are resulted in a curve fitting process are listed in Table 1.

Table 1. Stiffness coefficients of the nonlinear traction rod.

Symbol	Value	Unit
k_1	2.77×10^4	N.m^{-1}
k_2	0	N.m^{-2}
k_3	1.856×10^{12}	N.m^{-3}
k_4	13.56	N.m^{-4}
k_5	-2.128×10^{17}	N.m^{-5}
k_6	-9.858×10^5	N.m^{-6}
k_7	9.917×10^{21}	N.m^{-7}
k_8	2.194×10^{10}	N.m^{-8}
k_9	-1.622×10^{26}	N.m^{-9}

2.2 The analytical model of the vehicle with a flexible carbody

The results of the modal analysis of the Shinkansen high-speed railway vehicle carbody reported by Takigami and Tomioka (2007) revealed that its carbody behaves approximately like a free-free beam on its first and second bending modes and on its first twisting mode, which has natural frequencies of 9.84, 15.12, and 13.42 Hz, respectively. The carbody is subjected to the vertical forces applied by the secondary vehicle suspensions and the bending moments from the traction rods. The bending moment is assumed as a coupled vertical force, as in Figure 4. To avoid complexity, only the bending moments associated with the traction rod stiffness are presented in Figure 4. Δ represents the small distance between the coupled forces that generate the bending moment as in Equations (6) & (7).

$$M_{ti} = f_{ti} h_{tc} = F_{ti} \Delta, \tag{6}$$

$$M_{yj} = f_{yj} h_{yc} = F_{yj} \Delta, \tag{7}$$

where M_{ti} and M_{yi} are the bending moments that are generated by the longitudinal forces arising from within the traction rod and the yaw damper, respectively.

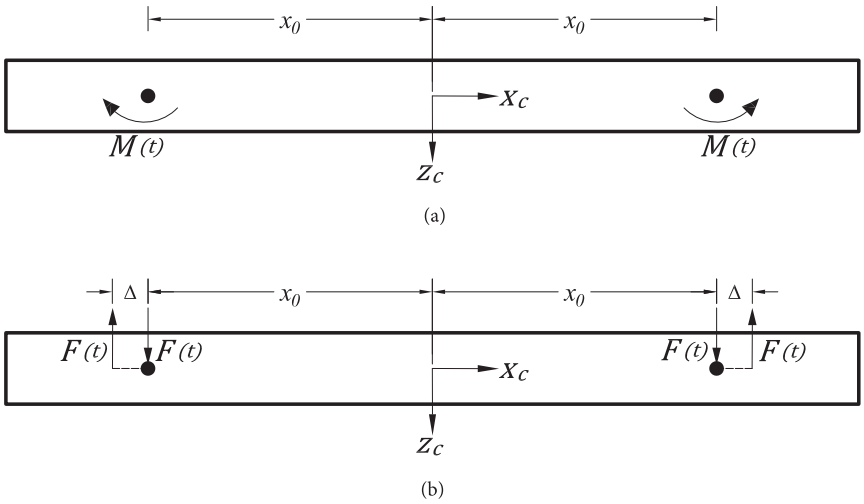

Figure 4. Dynamic model for a beam under bending moment; a) Beam under bending moments and b) Beam under coupled vertical forces.

For a beam of length L, density ρ, and cross-section area A, the equation for bending deformation can be expressed as:

$$\begin{aligned}\ddot{q}_{nb}(t) + 2\xi_{nb}\omega_{nb}\dot{q}_{nb}(t) + \omega_{nb}^2 q(t) = \frac{1}{\rho AL}\Big[&-f_{zsfr}X_{nb}(l_f) - f_{zsfl}X_{nb}(l_f) - f_{zsrr}X_{nb}(l_r) \\ &- f_{zsrl}X_{nb}(l_r) + \frac{f_{tf}h_{tc}}{\Delta}\left\{X_{nb}(l_{tf}+\Delta) - X_{nb}(l_{tf})\right\} - \frac{f_{tr}h_{tc}}{\Delta}\left\{X_{nb}(l_{tr}+\Delta) - X_{nb}(l_{tr})\right\} \\ &+ \frac{f_{yf}h_{yc}}{\Delta}\left\{X_{nb}(l_{yf}+\Delta) - X_{nb}(l_{yf})\right\} - \frac{f_{yr}h_{yc}}{\Delta}\left\{X_{nb}(l_{yr}+\Delta) - X_{nb}(l_{yr})\right\}\Big]\end{aligned} \tag{8}$$

While f_{zsij} are the vertical forces that are generated by the secondary suspension system, sub-index i refers to the front or the rear bogies and should be replaced by f or r, respectively. Sub-index j refers to the right or the left side of the carbody and should be replaced by r or l, respectively. By finding the limits for the last four terms on the right side of Equation (8) and by calculating the derivative, it can be simplified as

$$\begin{aligned}\ddot{q}_{nb}(t) + 2\xi_{nb}\omega_{nb}\dot{q}_{nb}(t) + \omega_{nb}^2 q(t) = \frac{1}{\rho AL}\Big\{&-f_{zsfr}X_{nb}(l_f) - f_{zsfl}X_{nb}(l_f) - f_{zsrr}X_{nb}(l_r)\Big\} \\ &- f_{zsrl}X_{nb}(l_r) + f_{tf}h_{tc}X'_{nb}(l_{tf}) - f_{tr}h_{tc}X'_{nb}(l_{tr}) + f_{yf}h_{yc}X'_{nb}(l_{yf}) - f_{yr}h_{yc}X'_{nb}(l_{yr})\Big\}\end{aligned} \tag{9}$$

$$\omega_{nb}^2 = \beta_{nb}^4 \frac{EI}{\rho A}, \quad 2\zeta_{nb}\omega_{nb} = \beta_{nb}^4 \frac{\mu I}{\rho A}, \tag{10}$$

For modeling the twisting vibration of the carbody, a free-free beam model with length L, polar moment of inertia J, and density ρ the following equation can be used.

$$\ddot{q}_{m\varphi}+2\xi_{m\varphi}\omega_{m\varphi}\dot{q}_{m\varphi}+\omega_{m\varphi}^{2}q_{m\varphi}=\frac{1}{\rho JL}\Big\{-bf_{szfr}X_{m\varphi}(L_f)+bf_{szfl}X_{m\varphi}(L_f)-bf_{zsrr}X_{m\varphi}(L_r)$$
$$-bf_{zsrr}X_{m\varphi}(L_r)+bf_{zsrl}X_{m\varphi}(L_r)\Big\} \tag{11}$$

There is no detailed information on Shinkansen's (series 100) elastic vibration characteristics. Therefore, in this study, the damping coefficients for the carbody's flexural modes are obtained through a try and error procedure. The practice included finding the best fit between the outcome of the modeling and the reported measured data by Tomioka and Takigami (2010). The results are presented in Table A-1.

The vertical movement of each point on the carbody can be calculated as

$$z_c(x,y,t)=z_c^r(t)+(x-\frac{L}{2})\theta_c(t)+y\,\varphi_c^r(t)+\sum_{n=1}^{N}X_{nb}(x)q_{nb}(t)+\sum_{m=1}^{M}X_{m\varphi}(x)q_{m\varphi}(t) \tag{12}$$

where $z_c^r(t)$, $\theta_c(t)$, and $\varphi_c^r(t)$ are the bounce, pitch and roll of the carbody, respectively. The equations of motion of the carbody are:

$$m_c\ddot{z}_c^r=-f_{zsfr}-f_{zsfl}-f_{zsrr}-f_{zsrl} \tag{13}$$

$$I_{cy}\ddot{\theta}_c=l_cf_{zsfr}+l_cf_{zsfl}-l_cf_{zsrr}-l_cf_{zsrl}-h_{tc}f_{tf}-h_{tc}f_{tr}-h_{yc}f_{yf}-h_{yc}f_{yr} \tag{14}$$

$$I_{cx}\ddot{\varphi}_c=-bf_{zsfr}+bf_{zsfl}-bf_{zsrr}+bf_{zsrl} \tag{15}$$

where f_{ti}, f_{yi}, and f_{zsij} represent the forces that are defined as;

$$f_{ti}=k_t\delta_{ti},$$
$$\delta_{ti}=x_c+h_{tc}\sum_{n=1}^{N}X'_{nb}(l_{ti})q_{nb}+h_{tc}\theta_c-x_{bi}, \tag{16}$$

$$f_{yi}=k_y\delta_{yi}+c_y\dot{\delta}_{yi},$$
$$\delta_{yi}=x_c+h_{yc}\sum_{n=1}^{N}X'_{nb}(l_{yi})q_{nb}+h_{yc}\theta_c-x_{bi}, \tag{17}$$

$$\begin{aligned}
f_{zsfr}&=k_{zs}\Big[\Big(z_c+\sum X_{nb}(l_f)q_{nb}-l_c\theta_c+b\Big(\varphi_c+\sum X_{m\varphi}(l_f)q_{m\varphi}\Big)\Big)-\big(z_{bf}+b\varphi_{bf}\big)\Big]\\
&\quad+c_{zs}\Big[\Big(\dot{z}_c+\sum X_{nb}(l_f)\dot{q}_{nb}-l_c\dot{\theta}_c+b\Big(\dot{\varphi}_c+\sum X_{m\varphi}(l_f)\dot{q}_{m\varphi}\Big)\Big)-\big(\dot{z}_{bf}+b\dot{\varphi}_{bf}\big)\Big]\\
f_{zsfl}&=k_{zs}\Big[\Big(z_c+\sum X_{nb}(l_f)q_{nb}-l_c\theta_c-b\Big(\varphi_c+\sum X_{m\varphi}(l_f)q_{m\varphi}\Big)\Big)-\big(z_{bf}-b\varphi_{bf}\big)\Big]\\
&\quad+c_{zs}\Big[\Big(\dot{z}_c+\sum X_{nb}(l_f)\dot{q}_{nb}-l_c\dot{\theta}_c-b\Big(\dot{\varphi}_c+\sum X_{m\varphi}(l_f)\dot{q}_{m\varphi}\Big)\Big)-\big(\dot{z}_{bf}-b\dot{\varphi}_{bf}\big)\Big]\\
f_{zsrr}&=k_{zs}\Big[\Big(z_c+\sum X_{nb}(l_r)q_{nb}+l_c\theta_c+b\Big(\varphi_c+\sum X_{m\varphi}(l_r)q_{m\varphi}\Big)\Big)-\big(z_{br}+b\varphi_{br}\big)\Big]\\
&\quad+c_{zs}\Big[\Big(\dot{z}_c+\sum X_{nb}(l_r)\dot{q}_{nb}+l_c\dot{\theta}_c+b\Big(\dot{\varphi}_c+\sum X_{m\varphi}(l_r)\dot{q}_{m\varphi}\Big)\Big)-\big(\dot{z}_{br}+b\dot{\varphi}_{br}\big)\Big]\\
f_{zsrl}&=k_{zs}\Big[\Big(z_c+\sum X_{nb}(l_r)q_{nb}+l_c\theta_c-b\Big(\varphi_c+\sum X_{m\varphi}(l_r)q_{m\varphi}\Big)\Big)-\big(z_{br}-b\varphi_{br}\big)\Big]\\
&\quad+c_{zs}\Big[\Big(\dot{z}_c+\sum X_{nb}(l_r)\dot{q}_{nb}+l_c\dot{\theta}_c-b\Big(\dot{\varphi}_c+\sum X_{m\varphi}(l_r)\dot{q}_{m\varphi}\Big)\Big)-\big(\dot{z}_{br}-b\dot{\varphi}_{br}\big)\Big]
\end{aligned} \tag{18}$$

Equations of motion of the bogies are;

$$m_b \ddot{z}_{bi} = f_{zsir} + f_{zsil} - f_{zpifr} - f_{zpifl} - f_{zpirr} - f_{zpirl} \tag{19}$$

$$I_{by} \ddot{\theta}_{bi} = l_w f_{zpifr} + l_w f_{zpifl} - l_w f_{zpirr} - l_w f_{zpirl} + f_{ti} h_{tb} + f_{yi} h_{yb} - 2h_{wb} k_{xp} x_{bi} \tag{20}$$

$$I_{bx} \ddot{\varphi}_{bi} = bf_{zsir} - bf_{zsil} - bf_{zpifr} + bf_{zpifl} - bf_{zpirr} + bf_{zpirl} \tag{21}$$

where f_{zpijk} represent the forces within the primary suspension system between the bogie and the wheelsets, which are defined as:

$$\begin{aligned}
f_{zpifr} &= k_{zp}\left[\left(z_{bi} - l_w \theta_{bi} + b\varphi_{bi}\right) - \left(z_{wif} + b\varphi_{wif}\right)\right] \\
&\quad + c_{pz}\left[\left(\dot{z}_{bi} - l_w \dot{\theta}_{bi} + b\dot{\varphi}_{bi}\right) - \left(\dot{z}_{wif} + b\dot{\varphi}_{wif}\right)\right] \\
f_{zpifl} &= k_{zp}\left[\left(z_{bi} - l_w \theta_{bi} - b\varphi_{bi}\right) - \left(z_{wif} - b\varphi_{wif}\right)\right] \\
&\quad + c_{pz}\left[\left(\dot{z}_{bi} - l_w \dot{\theta}_{bi} - b\dot{\varphi}_{bi}\right) - \left(\dot{z}_{wif} - b\dot{\varphi}_{wif}\right)\right] \\
f_{zpirr} &= k_{zp}\left[\left(z_{bi} + l_w \theta_{bi} + b\varphi_{bi}\right) - \left(z_{wir} + b\varphi_{wir}\right)\right] \\
&\quad + c_{pz}\left[\left(\dot{z}_{bi} + l_w \dot{\theta}_{bi} + b\dot{\varphi}_{bi}\right) - \left(\dot{z}_{wir} + b\dot{\varphi}_{wir}\right)\right] \\
f_{zpirl} &= k_{zp}\left[\left(z_{bi} + l_w \theta_{bi} - b\varphi_{bi}\right) - \left(z_{wir} - b\varphi_{wir}\right)\right] \\
&\quad + c_{pz}\left[\left(\dot{z}_{bi} + l_w \dot{\theta}_{bi} - b\dot{\varphi}_{bi}\right) - \left(\dot{z}_{wir} - b\dot{\varphi}_{wir}\right)\right]
\end{aligned} \tag{22}$$

The Equations (23) and (24) present the motion of the wheelsets;

$$m_w \ddot{z}_{wij} = f_{pijr} + f_{pijl} - (N_r + N_l)_{wij} \tag{23}$$

$$I_{wx} \ddot{\phi}_{wij} = bf_{pijr} - bf_{pijl} - b_w (N_r - N_l)_{wij} \tag{24}$$

To obtain the equation of motion for the wheelsets of each bogie, the sub-indexes i and j should be replaced by f, and r. N_r and N_l are the normal wheel/rail contact forces corresponding to the right and the left sides, respectively. These forces are calculated by using the Hertzian contact theory with the assumption of linear equivalent spring; as follow;

$$\begin{aligned}
N_r &= k_{hz}\delta_r, \quad \delta_r = z_w + b_w \phi_w - z_{0r} \\
N_l &= k_{hz}\delta_l, \quad \delta_l = z_w - b_w \phi_w - z_{0l}
\end{aligned} \tag{25}$$

All parameters are introduced in Table A-1 in the appendix.

3 The test rig setup

3.1 The scaling approach

The first step to determine a system of similarity is the definition of the length scale factor ($\varphi_l = l_1/l_0$), where l_1 and l_0 are the lengths of the full scale and the scaled model, respectively. Similarly, the time scaling factor is $\varphi_t = t_1/t_0$. Further instructions regarding the scaling method can be found in (Iwnicki, 2006).

Depending on the purposes of the studies, the scaling factor for each system can be different. While attempting to highlight the phenomenon of interest, scaling should not neglect the geometrical and physical constraints and should not adversely interfere with the facts about the real subject. In the present research, since the main aim of the scaled test is to detect the dynamic interaction phenomenon; therefore, with the aim of reducing the cost without hurting the physical facts, a reasonably sizeable scaling factor of 1:24.5 is selected.

Subsequently, an experimental test rig on this scale based on a simplified model of a Shinkansen high-speed railway vehicle is made. This choice of equipment also conforms to the space limitations within the laboratory. Thus,

$$\varphi_l = 24.5 \tag{26}$$

$$\varphi_v = 24.5, \tag{27}$$

$$\varphi_a = 24.5, \tag{28}$$

The specifications of the full-scale and the scaled models are as in Table 2.

Table 2. Properties of full-scale and scaled models.

Parameter	Full-scale	Scaled
Carbody mass (kg)	16900	1.149
Bogie frame mass (kg)	2580	0.175
Carbody length (m)	24.5	1
Longitudinal distance between the two bogie centers (m)	17.5	0.7143
Longitudinal distance between the wheelsets (m)	1.25	0.051
Stiffness of primary suspension ($N.m^{-1}$)	19700000	1339
Stiffness of secondary suspension ($N.m^{-1}$)	2560000	174.1

3.2 The test setup

Figures 5 and 6 present a schematic of the scaled model and the pictures for the test rig arrangement in the laboratory. Two Piezotronic modal shakers of type JZK-20 from Sinocera/China are used to excite the model. Each shaker excites one of the two bogies of the vehicle. Since the main aim of the test is the illustration of the bogie-carbody dynamic interaction, the use of two shakers instead of four does not interfere with the main aim of the research. This excitation is programmed to be digitally generated and then converted to an analog signal by using a digital to analog (D/A) converter card (USB-AD16f- BMCM). The analog signal then needs to be amplified before being fed to the modal shakers. The modal shaker for the rear bogie receives the same track excitation signals with a time delay respective to the one for the front bogie. This time delay is required to mimic the vehicle speed of travel. When the scaled model is excited, an acquisition system registers the longitudinal acceleration of the bogie frame and the vertical acceleration of the carbody center. Two types of accelerometers coded as CA-YD-186 and CA-DR-3001 both from Sinocera/China are used for the measurements.

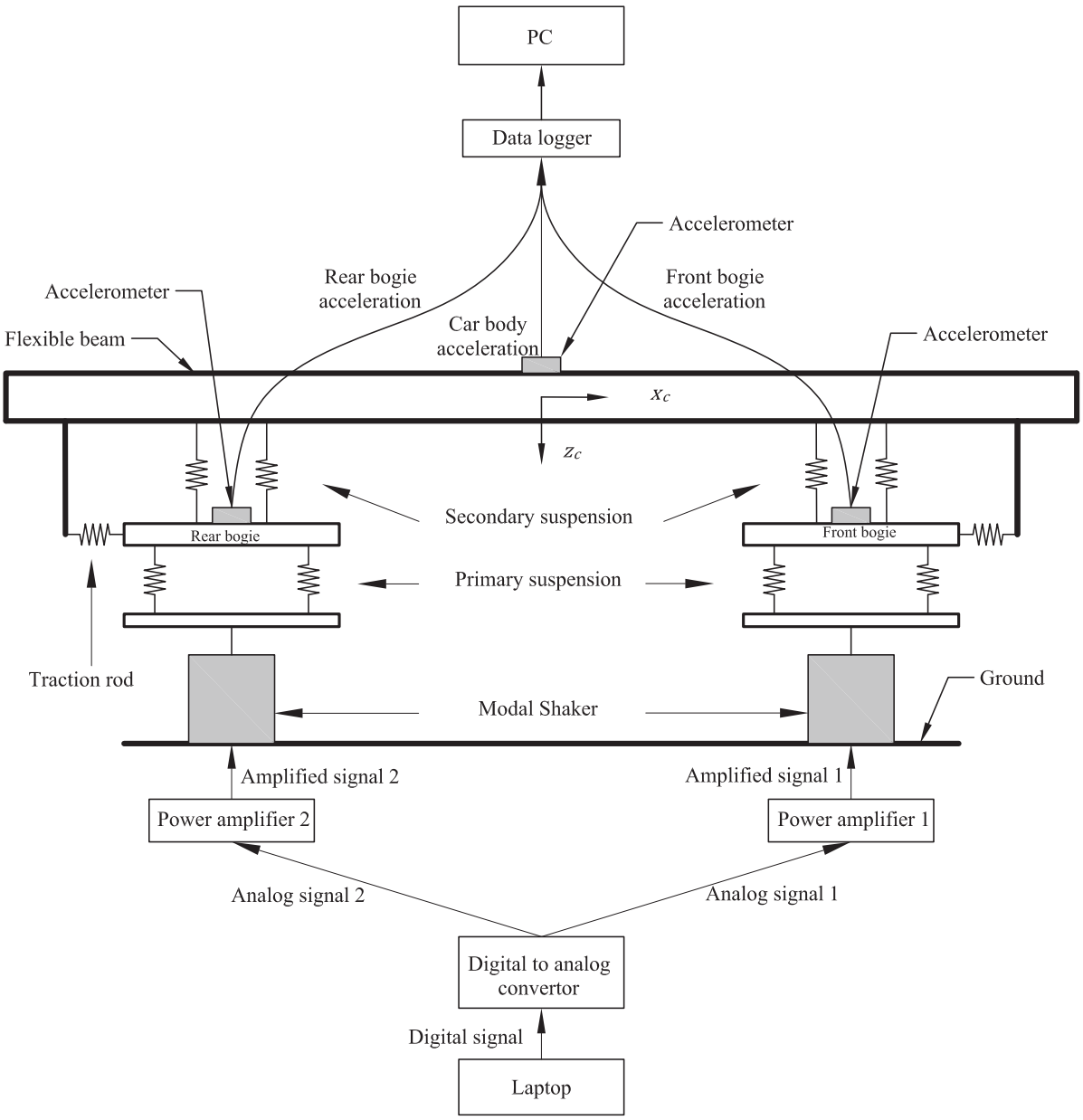

Figure 5. Schematic of the scaled model of a high-speed railway vehicle.

The excitation force applied by the shakers is computed based on a non-deformable track and a track irregularity in compliance with the class six of track irregularities that is recommended by the Federal Railroad Administration (FRA) (Garg and Dukkipati, 1984) of the USA. The same input that is applied to the theoretical model of the full system is also applied to the scaled model.

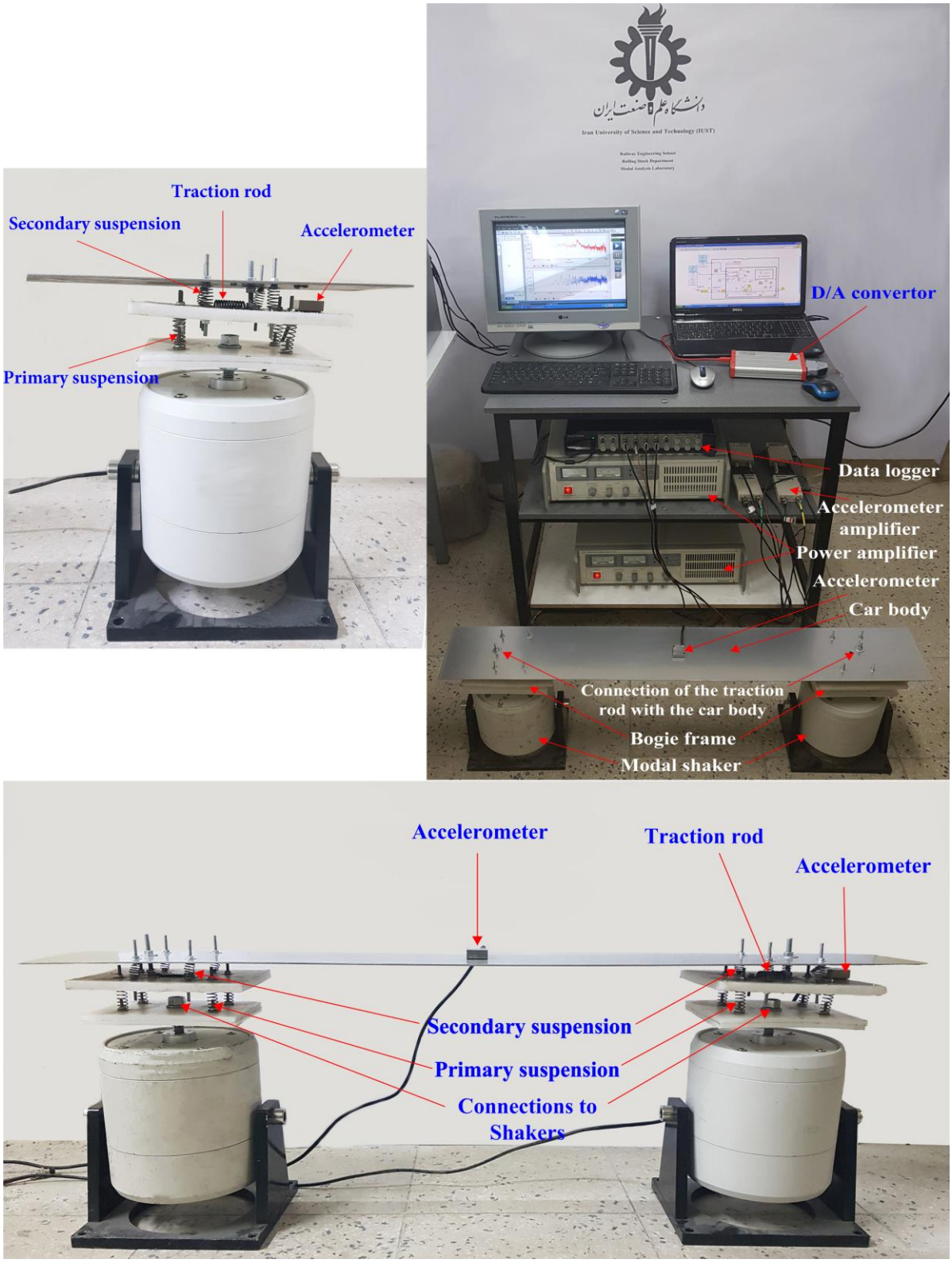

Figure 6. Test rig arrangement on a scale of 1:24.5.

3.3 The analytical model of the scaled vehicle

A theoretical model of the scaled model is constructed that consists of nine degrees of freedom associated with rigid body motions, including the vertical and longitudinal motions and pitching of the carbody and the bogie frames. It also contains three flexible bending modes of the carbody. Since the linearity or nonlinearity of the traction rod element does not

affect the occurrence of the bogie-carbody dynamic interaction phenomenon; therefore, at this stage, the traction rod element is assumed as a linear element.

The equations of motion of the carbody are

$$m_c\ddot{x}_c + 2k_t x_c - k_t x_{bf} - k_t x_{br} + k_t h_c \sum_{n=1}^{3}\left[X'_{nb}(l_{tf}) + X'_{nb}(l_{tr})\right]q_{nb} = 0 \tag{29}$$

$$m_c\ddot{z}_c + 2k_{sz} z_c - k_{sz} z_{bf} - k_{sz} z_{br} + k_{sz} \sum_{n=1}^{3}\left[X_{nb}(l_f) + X_{nb}(l_r)\right]q_{nb} = 0 \tag{30}$$

$$\begin{aligned} &J_c\ddot{\theta}_c + 2k_t h_c x_c + 2k_{sz} l_c^2\theta_c - k_t h_{tc} x_{bf} + k_{sz} l_c z_{bf} - k_t h_{tc} x_{br} - k_{sz} l_c z_{br} \\ &-k_{sz} l_c \sum_{n=1}^{3}\left[X_{nb}(l_f) - X_{nb}(l_r)\right]q_{nb} + k_t h_{tc}^2 \sum_{n=1}^{3}\left[X'_{nb}(l_{tf}) + X'_{nb}(l_{tr})\right]q_{nb} = 0 \end{aligned} \tag{31}$$

$$\begin{aligned} &\ddot{q}_{nb} + 2\xi_{nb}\omega_{nb}\dot{q}_{nb} + \omega_{nb}^2 q_{nb} = \frac{1}{m_c}\Big\{-k_t h_{tc}\left(X'_{nb}(l_{tf}) + X'_{nb}(l_{tr})\right)x_c \\ &-k_{sz}\left(X_{nb}(l_f) + X_{nb}(l_r)\right)z_c + k_{sz} l_c\left(X_{nb}(l_f) - X_{nb}(l_r)\right)\theta_c \\ &-k_{sz}\left[X_{nb}(l_f)\sum_{n=1}^{3}X_{nb}(l_f)q_{nb} + X_{nb}(l_r)\sum_{n=1}^{3}X_{nb}(l_r)q_{nb}\right] \\ &+k_{sz}X_{nb}(l_f)z_{bf} + k_{sz}X_{nb}(l_r)z_{br} + k_t h_{tc}X'_{nb}(l_{tf})x_{bf} + k_t h_{tc}X'_{nb}(l_{tr})x_{br} \\ &-k_t h_{tc}^2\left[X'_{nb}(l_{tf})\sum_{n=1}^{3}X'_{nb}(l_{tf})q_{nb} + X'_{nb}(l_{tr})\sum_{n=1}^{3}X'_{nb}(l_r)q_{nb}\right]\Big\} \end{aligned} \tag{32}$$

Also, the equations of motion of the front and the rear bogies are

$$m_b\ddot{x}_{bf} - k_t x_c + (k_t + 2k_{px})x_{bf} + k_t h_{tc}\sum_{n=1}^{3}X'_{nb}(l_{tf})q_{nb} = 0 \tag{33}$$

$$m_b\ddot{z}_{bf} - k_{sz} z_c + k_{sz} l_c\theta_c + (k_{sz} + 2k_{pz})z_{bf} + k_{sz}\sum_{n=1}^{3}X_{nb}(l_f)q_{nb} = 2k_{pz} z_{0f} \tag{34}$$

$$J_b\ddot{\theta}_{bf} - k_t h_{tb} x_c + k_t h_{tb} x_{bf} + 2l_w^2 k_{pz}\theta_{bf} - k_t h_{tc} h_{tb}\sum_{n=1}^{3}X'_{nb}(l_{tf})q_{nb} = 0 \tag{35}$$

$$m_b\ddot{x}_{bf} - k_t x_c + (k_t + 2k_{px})x_{br} + k_t h_{tc}\sum_{n=1}^{3}X'_{nb}(l_{tr})q_{nb} = 0 \tag{36}$$

$$m_b\ddot{z}_{br} - k_{sz} z_c - k_{sz} l_c\theta_c + (k_{sz} + 2k_{pz})z_{br} + k_{sz}\sum_{n=1}^{3}X_{nb}(l_r)q_{nb} = 2k_{pz} z_{0r} \tag{37}$$

$$J_b\ddot{\theta}_{br} - k_t h_{tb} x_c + k_t h_{tb} x_{br} + 2l_w^2 k_{pz}\theta_{br} - k_t h_{tc} h_{tb}\sum_{n=1}^{3}X'_{nb}(l_{tr})q_{nb} = 0 \tag{38}$$

4 Frequency-domain analysis of the nonlinear system

In this research, the equivalent linearization method is implemented to convert the nonlinear system presented in Section 2 to an equivalent linear one. A brief explanation of the solution approach is presented. Further details about this method are available in (Roberts and Spanos, 2003). Consider a matrix form for a nonlinear dynamic system in which only its stiffness matrix is nonlinear,

$$\mathbf{M}\ddot{\mathbf{x}}(t)+\mathbf{C}\dot{\mathbf{x}}(t)+\mathbf{K}\mathbf{x}(t)+\mathbf{\Phi}(\mathbf{x}(t))=\mathbf{q}(t), \tag{39}$$

where **M**, **C**, and **K** are the mass, damping, and stiffness matrices, respectively. Φ is a vector that contains the nonlinear behavior of the system concerning the displacement. $q(t)$ is a vector that contains the random excitation of the system. A linear system equivalent to the nonlinear system in Equation (39) can be considered as

$$\mathbf{M}\ddot{\mathbf{x}}(t)+\mathbf{C}\dot{\mathbf{x}}(t)+(\mathbf{K}+\mathbf{K}_e)\mathbf{x}=\mathbf{q}(t), \tag{40}$$

where $\mathbf{K}_e$ should be determined in such a way that the Euclidean norm of the error vector

$$\mathbf{e}=\mathbf{M}\ddot{\mathbf{x}}+\mathbf{C}\dot{\mathbf{x}}+\mathbf{K}\mathbf{x}+\mathbf{\Phi}(\mathbf{x})-[\mathbf{M}\ddot{\mathbf{x}}+\mathbf{C}\dot{\mathbf{x}}+(\mathbf{K}+\mathbf{K}_e)\mathbf{x}]=\mathbf{\Phi}(\mathbf{x})-\mathbf{K}_e\mathbf{x}. \tag{41}$$

is minimized. It can be proved that the minimization condition of the error vector in Equation (41) is (Roberts and Spanos, 2003);

$$k_{ij}^{e}=E[\frac{\partial\Phi_i}{\partial\mathbf{x}_j}], \tag{42}$$

where E represents expected value function of the corresponding argument. The nonlinear vector **Φ** is defined as;

$$\mathbf{\Phi}(\mathbf{x})=\begin{Bmatrix} f_{tfNL}+f_{trNL} \\ 0 \\ h_{tc}(f_{tfNL}+f_{trNL}) \\ 0 \\ -f_{tfNL} \\ 0 \\ -h_{tb}f_{tfNL} \\ 0 \\ -f_{trNL} \\ 0 \\ -h_{tb}f_{trNL} \\ 0 \\ [0]_{8\times1} \\ 2h_{tc}[f_{tfNL}X_1'(l_{tf})+f_{trNL}X_1'(l_{tr})]/m \\ 2h_{tc}[f_{tfNL}X_2'(l_{tf})+f_{trNL}X_2'(l_{tr})]/m \\ 0 \end{Bmatrix} \tag{43}$$

Considering Equation (5), the force due to the length alteration of the traction rod element can be divided into two linear and nonlinear parts, while the nonlinear part is;

$$f_{tiNL} = k_9\delta_{ti}^9 + k_8\delta_{ti}^7 \,|\,\delta_{ti}\,| + k_7\delta_{ti}^7 + k_6\delta_{ti}^5 \,|\,\delta_{ti}\,| + k_5\delta_{ti}^5 + k_4\delta_{ti}^3 \,|\,\delta_{ti}\,| + k_3\delta_{ti}^3 + k_2\delta_{ti}\,|\delta_{ti}|, \tag{44}$$

There is interdependence between the components of the matrix $\mathbf{K}_e$ and the system response. Therefore, the calculation procedure for the components of $\mathbf{K}_e$ is based on a try and error procedure. To calculate the elements of system equivalent stiffness matrix ($\mathbf{K}_e$), if a polynomial form is assumed for the nonlinear part the solution procedure becomes faster.

5 Results and discussion

5.1 Validation of the dynamic model of the vehicle

The outcome of the analysis of the model vehicle by using the equivalent linearization method is compared with the time-domain solution of the nonlinear system and, also, with the results of a running test of a Shinkansen high-speed railway vehicle that was carried out by Tomioka and Takigami (2010). The specifications of the vehicle are provided in Table A-1.

For the vehicle speed of 300 km/h, and a class six of rail track irregularity of FRA classification, the vertical acceleration of the carbody floor are calculated and are presented in Figure 7.

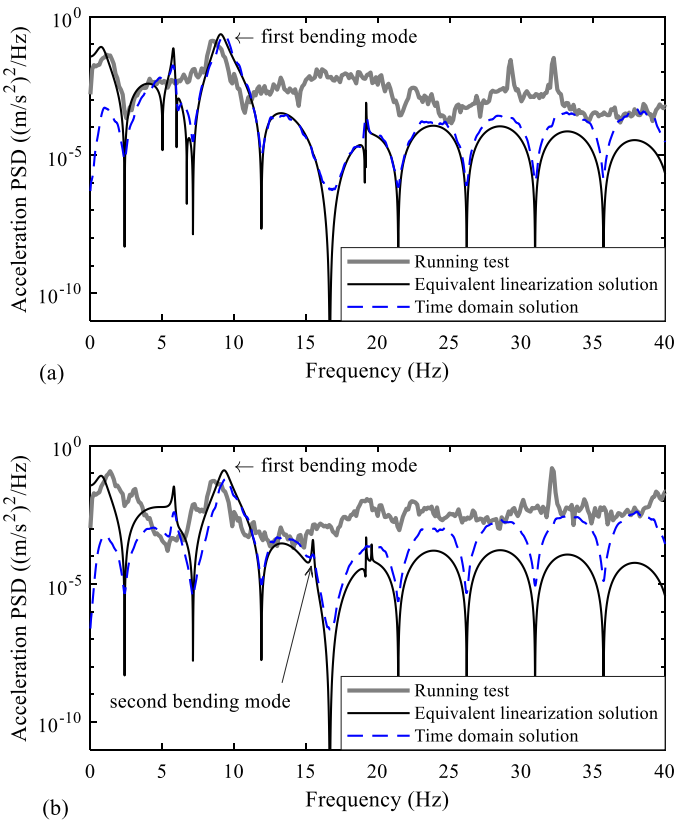

Figure 7. Comparison between measured acceleration (Tomioka and Takigami, 2010) and simulation results, a) acceleration at the center of the carbody floor, b) acceleration of the carbody floor at above the front bogie.

The excitation of the carbody's first bending mode at two selected points can be detected. These are presented by the peaks around its natural frequency of 9.84 Hz. However, the second bending mode of vibration only appears in the response of the carbody floor above the

front bogie. This was predictable since the second bending mode is not expected to be sensed at the center of the carbody due to its mode shape. There is also a proper matching between the simulation results and the running test results in the frequency range of 9 to 10 Hz, where the peak of vertical acceleration associated with the first bending mode of the carbody is located in this range. Besides, the results of the equivalent linearization solution method are consistent with the solution of the nonlinear system in the time domain. At about 20 Hz, a peak in the acceleration of the carbody floor is observed, which is related to the longitudinal stiffness of the traction rod. Without the presence of the traction rod, such a peak does not appear at all (Bokaeian et al., 2019). This peak is an indicator of the existence of the bogie-carbody dynamic interaction.

Notably, there are some differences between the running test and the simulation results for the full-scale case that are highlighted in Figure 7. The differences are observed, particularly at the frequencies higher than 15 Hz. These discrepancies arise from differences in the excitations of the models (track inputs). The other source of the discrepancy in the results can be attributed to the simplifications that are inherent to the simulated vehicle model.

5.2 The dynamic interaction phenomenon within the scaled model

In Figure 8(a), the vertical acceleration at the center of the carbody floor obtained through the analytical method of solution of the scaled model, and the experimental test results are compared for the speed of 12.25 km/h (equal to the speed of 300 km/h for the full-scale vehicle), while the traction rod is eliminated. The peak values are due to the bending modes of vibration and the rigid body modes of the carbody. The presence of some anti-peaks within the results for the vertical acceleration of the carbody is clear. These anti-peaks represent a phenomenon known as the bogie-base filtering effect (Bokaeian et al., 2019; Gong et al., 2012; Tomioka and Takigami, 2010). The agreement between the two sets of the results for the frequency range of 3 to 20 Hz is about 20%.

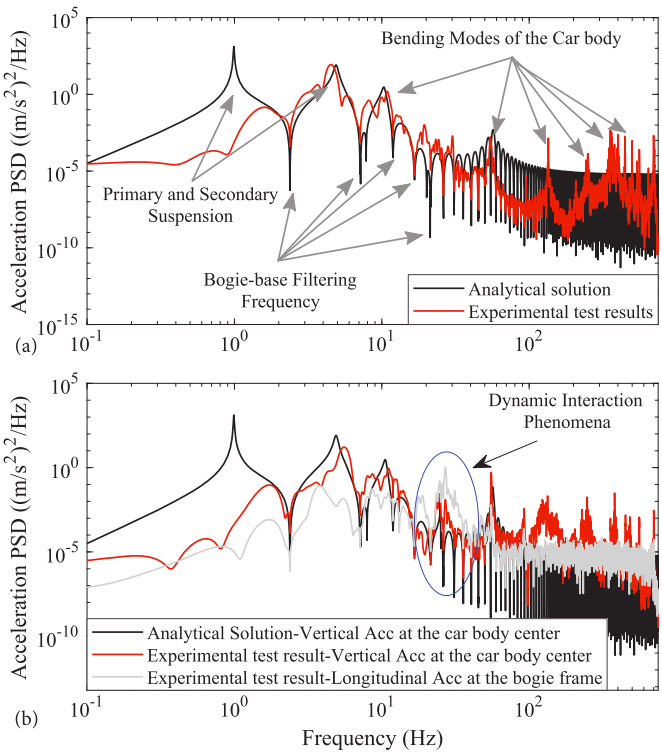

Figure 8. Acceleration of the scaled model; a) without traction rod and b) with traction rod.

Figure 8(b) presents the vertical acceleration of the carbody center obtained from the theoretical model and the measurements with the test rig while the traction rod is included. It also presents the longitudinal acceleration of the bogie in the presence of the traction rod. The presence of a peak in the longitudinal acceleration of the bogie at the frequency of 19 Hz is noticeable and is due to the traction rod stiffness. Such a peak does not appear in the vertical acceleration of the carbody and longitudinal acceleration of the bogie frame when the traction rod is removed from the model, as is presented in Figure 8(b). Also, this peak appears in the vertical acceleration of the carbody floor center, while it does not show up in the calculations when the traction rod is missing, in Figure 8. This outcome proves the existence of the bogie-carbody dynamic interaction phenomenon.

When comparing the results that are presented in Figure 8, the differences for the frequencies below 2 Hz are noticeable. This is due to the shortcoming of the modal shaker that could not be used to excite the scaled model in this frequency range below 2 Hz. Also, there are some differences at frequencies above 50 Hz. This is also due to using only the first three modes of the carbody's bending deformation for the dynamic simulations, while the test rig measurements contain the first 15 modes of the carbody's bending.

5.3 Improvement of the ride quality by optimizing the traction rod stiffness

In order to find the optimized stiffness of the traction rod (k_t), as the design variable that can improve the vehicle ride quality, an optimization method based on a genetic algorithm (GA) is used. The ride quality index is the function to be minimized. For calculating the ride quality index, the approach that is recommended within the standard EN 12299 is used. According to this standard, the ride quality index in the vertical direction, as the objective function in the optimization process is equal to;

$$N_{MV_z} = 6a_z^{w_d} \tag{45}$$

$a_z^{w_d}$ is the weighted acceleration which is calculated as:

$$a_z^{w_d} = \int_0^{\infty} a_z . W_b(f)df \ , \tag{46}$$

where W_b is the frequency weighting function of the vertical acceleration. Details of this filter can be found in EN12299 (2009). The stiffness of the traction rod that is used in the Shinkansen high-speed train is equal to 5.77×10^6 N/m. With the application of GA from MATLAB software, the optimized values of the traction rod stiffness to improve the ride quality index at various travel speeds are obtained. Figure 9 illustrates the effect of the traction rod stiffness on the ride quality index for various running speeds at the center and above the front bogie of the carbody floor. Optimizing the traction rod stiffness is considered as a passive method to improve the ride quality index. Therefore, it is vital to find the optimum value of the traction rod stiffness for the running speed that the vehicle tolerates for the most extended period of its travel. Such operating speed for the Shinkansen high-speed train (series 100) is 300 km/h. Therefore, the present research uses the running speed of 300 km/h to optimize its traction rod stiffness. From Figure 9, the best condition for the ride quality index is achieved with the traction rod stiffness equal to 3.65×10^7 N/m.

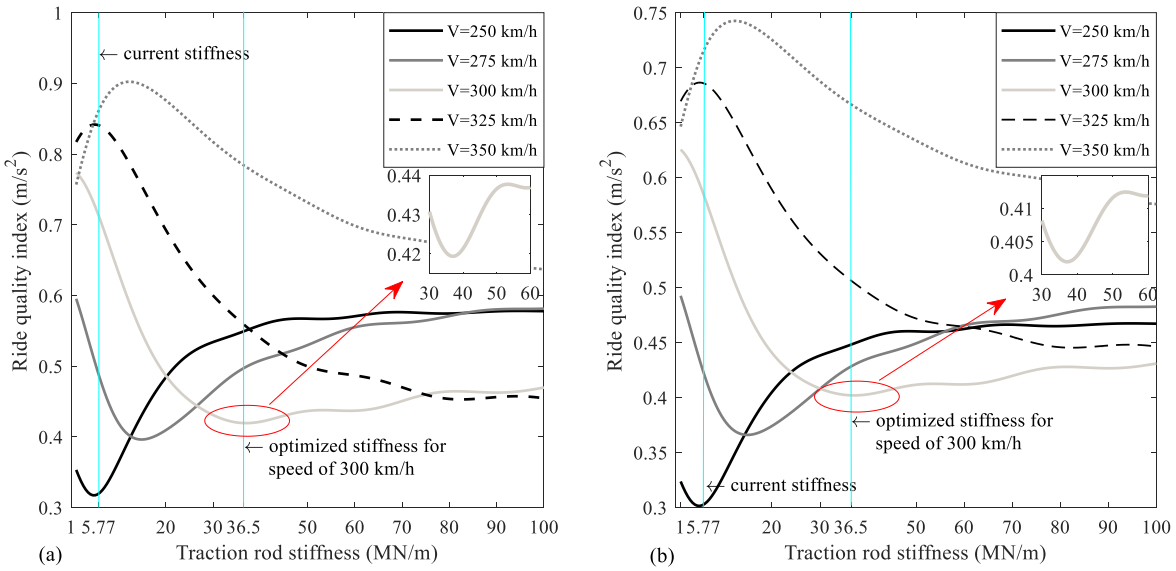

Figure 9. The effect of traction rod stiffness on ride quality index at various running speeds, a) at the center of carbody floor b) at above the front bogie of carbody floor.

The effect of the varying traction rod stiffness on the vertical acceleration and ride quality index at the center of the carbody floor is presented in Figure 10. Where with the application of the bogie-carbody dynamic interaction, the ride quality index advances for about 41 % at the speed of 300 km/h. At the speed of 300 km/h for $k_t = 5.77 \times 10^6$ N/m the ride index is equal to 0.7166 m/s^2 while for $k_t = 3.65 \times 10^7$ N/m, it is equal to 0.4207. However, at some other speed, such as the speed of 250 km/h, the ride quality index worsens. This is due to the bogie-base filtering effect that is presented in Figure 10(b). For the case where the stiffness of the traction rod element is optimized, at the speed of 300 km/h, the mutual effects of the anti-peaks related to the bogie-base filtering effect and the bogie-carbody dynamic interaction are enhanced and eliminate the first bending mode of the carbody. However, this does not happen at the speed of 250 km/h.

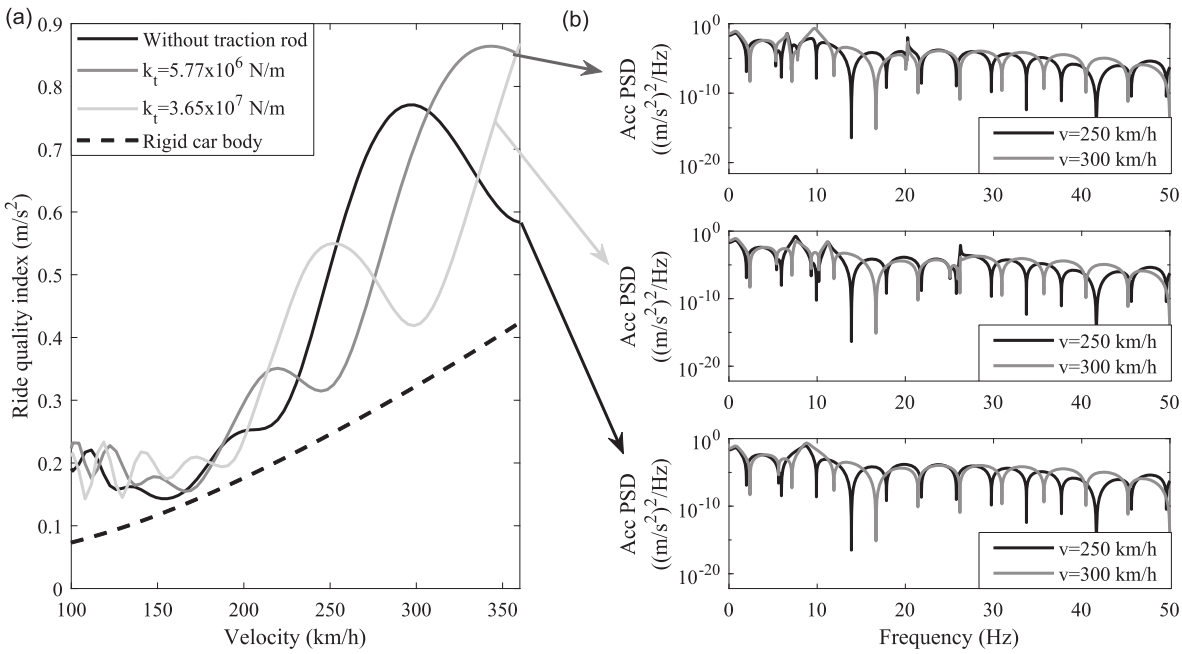

Figure 10. The effect of traction rod stiffness, a) Ride quality index at the center of carbody floor b) Vertical acceleration at the center of carbody floor.

Figure 11 presents the ride quality index above the bogie on the carbody floor. A similar scenario as in the center of the carbody floor as in Figure 10 appears in this case too. The ride quality index above the bogie on the carbody floor indicates a 20% improvement when compared with the center of the carbody floor. The ride quality index in the carbody walls worsens when compared with the centerline of the carbody. When moving away from the centerline of the carbody in the transversal direction, the acceleration associated with the roll of the carbody also affects its vertical acceleration (Bokaeian et al., 2019).

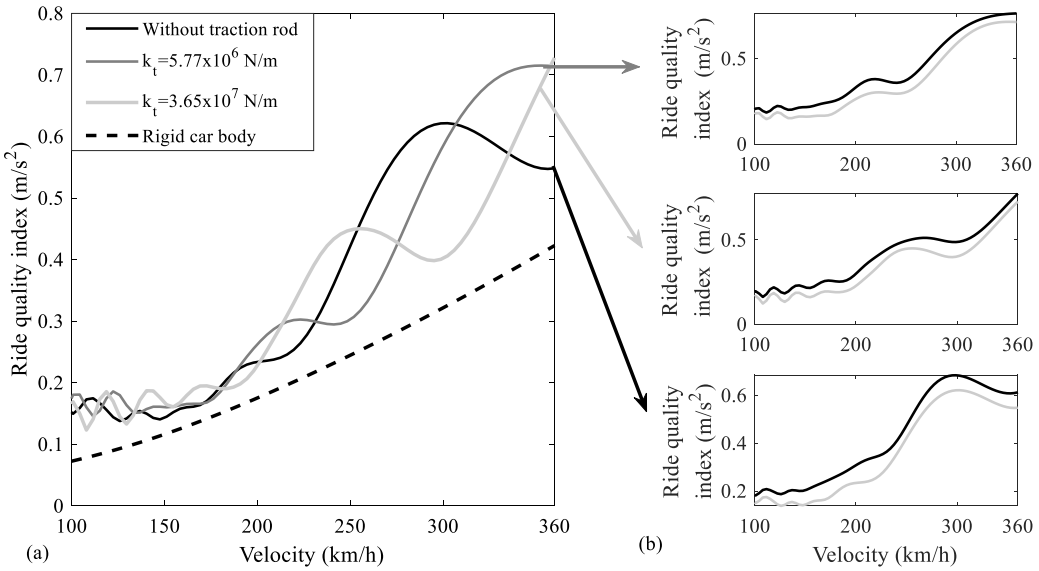

Figure 11. The effect of traction rod stiffness on ride quality, a) On carbody floor at above front bogie b) Comparison of ride quality at the centerline (gray) and near the wall (bold) of carbody floor at above front bogie.

6 Conclusions

This research was concerned with the effect of the flexural and twisting modes of the high-speed Shinkansen railway vehicle carbody on its ride quality index. To serve the purpose, the carbody is simulated as a free-free beam. Also, in order to investigate the effect of the bogie-carbody dynamic interaction, the traction rod element is assumed as a nonlinear element. The results are obtained by using the equivalent linearization method for the vehicle. Also, by setting up an experimental test rig, the phenomenon of the bogie-carbody dynamic interaction is practically established. The laboratory tests and the analytical estimations were performed for a range of vehicle speeds of travel with a higher limit of 360 km/h. The rail track irregularity of class six of FRA classification is used for demonstration purposes. The optimization method of the Genetic Algorithm is used to acquire the optimized stiffness for the traction rod element that can advance the vehicle ride quality index. The equivalent linearization method is used to estimate the dynamic behavior of the high-speed railway vehicle, and the outcome displayed a decent agreement with the time-domain solution of the nonlinear dynamic system. The presence of some peak values within the frequency response of the vertical acceleration of the carbody relates to the stiffness of the traction rod, indicating that there is a bogie-carbody dynamic interaction. Such interaction was also observed from the measurements that were taken from the scaled experimental test setup replicating a high-speed railway vehicle. With the application of the optimized nonlinear traction rod element, the results of the simulations prove 41 percent improvement in the ride quality index at the travel speed of 300 km/h.

Acknowledgments

The authors would like to express great appreciation to Professor Takahiro Tomioka from Akita Prefectural University for valuable and constructive suggestions during this research. The third author would also like to acknowledge the funds provided by the NVTRail project (Noise and Vibrations induced by railway traffic in tunnels: an integrated approach), funded by FEDER funds through COMPETE2020 and by national funds (PIDDAC) through FCT/MCTES, with grant reference POCI-01-0145-FEDER-029577; and by the VIBWAY project (Fast computational tool for railway-induced vibrations and re-radiated noise assessment), with reference RTI2018-096819-B-I00, supported by the Ministerio de Ciencia e Innovación, Retos de Investigación 2018.

References

Akiyama Y, Tomioka T, Takigami T, et al. (2019) A three-dimensional analytical model and parameter determination method of the elastic vibration of a railway vehicle carbody. *Vehicle System Dynamics* 55: 545-568.

Bokaeian V, Rezvani MA and Arcos R. (2019) The coupled effects of bending and torsional flexural modes of a high-speed train car body on its vertical ride quality. *Proceedings of the Institution of Mechanical Engineers, Part K: Journal of Multi-body Dynamics* 233: 979-993.

Carlbom P. (2000) Carbody and passenger in rail vehicle dynamics. *Department of Vehicle Engineering.* Royal Institue of Technology.

EN12299 B. (2009) Railway Applications. Ride Comfort for Passengers. Measurement and Evaluation. *BS EN 12299.*

Garg VK and Dukkipati RV. (1984) *Dynamics of Railway Vehicle Systems,* New York: Academic Press.

Gong D, Wang K, Duan Y, et al. (2019) Car body floor vibration of high-speed railway vehicles and its reduction. *Journal of Low Frequency Noise, Vibration and Active Control*.

Gong D, Zhou Js and Sun Wj. (2012) On the resonant vibration of a flexible railway car body and its suppression with a dynamic vibration absorber. *Journal of Vibration and Control* 19: 649–657.

Huang C, Zeng J, Luo G, et al. (2018) Numerical and experimental studies on the car body flexible vibration reduction due to the effect of car body-mounted equipment. *Proceedings of the Institution of Mechanical Engineers, Part F: Journal of Rail and Rapid Transit* 232: 103-120.

Iwnicki S. (2006) Handbook of Railway Vehicle Dynamics. In: Iwnicki S (ed).

Kamada T, Hiraizumi K and Nagai M. (2010) Active vibration suppression of lightweight railway vehicle body by combined use of piezoelectric actuators and linear actuators. *Vehicle System Dynamics* 48: 73-87.

Ling L, Zhang Q, Xiao X, et al. (2018) Integration of car-body flexibility into train–track coupling system dynamics analysis. *Vehicle System Dynamics* 56: 485-505.

Ripamonti F and Chiarabaglio A. (2019) A smart solution for improving ride comfort in high-speed railway vehicles. *Journal of Vibration and Control* 25: 1958-1973.

Roberts JB and Spanos PD. (2003) *Random vibration and statistical linearization,* New York: Courier Corporation.

Schandl G, Lugner P, Benatzky C, et al. (2007) Comfort enhancement by an active vibration reduction system for a flexible railway carbody. *Vehicle System Dynamics*.

Shi H and Wu P. (2016) Flexible vibration analysis for car body of high-speed EMU. *Journal of Mechanical Science and Technology* 30: 55-66.

Sugahara Y, Kazato A, Koganei R, et al. (2009) Suppression of vertical bending and rigid-body-mode vibration in railway vehicle carbody by primary and secondary suspension control: results of simulations and running tests using Shinkansen vehicle. *Rail and Rapid Transit*.

Sun W, Zhou J, Gong D, et al. (2016) Analysis of modal frequency optimization of railway vehicle car body. *Advances in Mechanical Engineering* 8: 1687814016643640.

Sun Y, Zhou J, Gong D, et al. (2017) A new vibration absorber design for under-chassis device of a high-speed train. *Shock and Vibration* 2017.

Takigami T and Tomioka T. (2007) Modal vibration analysis of recent railway vehicles. *Proceedings of the 12th Asia Pacific Vibration Conference (APVC2007).* Sapporo, Japan, 1-8.

Tomioka T and Takigami T. (2010) Reduction of bending vibration in railway vehicle carbodies using carbody–bogie dynamic interaction. *Vehicle System Dynamics* 48: 467-486.

Wang Q, Zeng J, Wei L, et al. (2018) Carbody vibrations of high-speed train caused by dynamic unbalance of underframe suspended equipment. *Advances in Mechanical Engineering* 10: 1687814018818969.

Wen Y, Sun Q, Zou Y, et al. (2019) Study on the vibration suppression of a flexible carbody for urban railway vehicles with a magnetorheological elastomer-based dynamic vibration absorber. *Proceedings of the Institution of Mechanical Engineers, Part F: Journal of Rail and Rapid Transit*: 0954409719865370.

Younesian D, Marjani SR and Esmailzadeh E. (2014) Importance of flexural mode shapes in dynamic analysis of high-speed trains traveling on bridges. *Journal of Vibration and Control* 20: 1565-1583.

Zhou J, Goodall R, Ren L, et al. (2009) Influences of car body vertical flexibility on ride quality of passenger railway vehicles. *Proceedings of the Institution of Mechanical Engineers, Part F: Journal of Rail and Rapid Transit* 223: 461-471.

Appendix A:

Table A-1. The technical specifications of the Shinkansen high-speed rail vehicle (series 100) (Tomioka and Takigami, 2010).

Symbol	Description	Value	unit
b	lateral displacement of the secondary suspension	2.2	m
b_w	half of the track gauge	0.7175	m
c_y	yaw damping coefficient of the secondary suspension per damper	8×10^6	$N.s.m^{-1}$
c_{zp}	vertical damping of the primary suspension per axle box	3.92×10^4	$N.s.m^{-1}$
c_{zs}	vertical damping of the secondary suspension at each side of the bogie	2.255×10^4	$N.s.m^{-1}$
f_{xpij}	longitudinal forces between the wheelset and the bogie frame which are related to the primary suspension	-	N
f_{ti}	longitudinal forces between the bogie frame and the car body which are related to the traction rod stiffness	-	N
f_{yi}	longitudinal forces between the bogie frame and the car body which are related to the yaw damper	-	N
f_{zpij}	vertical forces between the wheelset and the bogie frame which are related to the primary suspension	-	N
f_{zsijk}	vertical forces between the bogie frame and the car body which are related to the secondary suspension	-	N
h_{tc}	the vertical distance between the traction rod and the neutral axis of the car body	0.97	m
h_{yc}	the vertical distance between the yaw damper and the neutral axis of the car body	0.92	m
h_{tb}	the vertical distance between the traction rod and the neutral axis of the bogie frame	0.1	m
h_{yb}	the vertical distance between the yaw damper and the neutral axis of the bogie frame	0.05	m

h_{wb}	the vertical distance between the center of gravity of the wheelset and the neutral axis of the bogie frame	0.1	m
J_{bx}	moment of inertia of the bogie around x axis	1580	kg.m^2
J_{by}	moment of inertia of the bogie around y axis	2340	kg.m^2
J_{cx}	moment of inertia of the car body around x axis	2.32×10^4	kg.m^2
J_{cy}	moment of inertia of the car body around y axis	2.1×10^6	kg.m^2
k_{hz}	equivalent linear spring of the Hertzian contact	7.52×10^8	N.m^{-1}
k_{tL}	longitudinal stiffness of the linear traction rod per bogie	5.77×10^6	N.m^{-1}
k_{xp}	longitudinal stiffness of the primary suspension per wheelset	4.2×10^6	N.m^{-1}
k_y	stiffness of the yaw damper per damper	6.13×10^6	N.m^{-1}
k_{zp}	vertical stiffness of the primary suspension per axle box	9.85×10^5	N.m^{-1}
k_{zs}	vertical stiffness of the secondary suspension at each side of the bogie	1.28×10^6	N.m^{-1}
l	length of the car body	24.5	m
l_b	half distance between the two bogie centers	8.75	m
l_c	the longitudinal position of the center of the car body measured from its rear end	12.25	m
l_f	the longitudinal position of the front secondary suspension on the car body from its rear end	21	m
l_r	the longitudinal position of the rear secondary suspension on the car body from its rear end	3.5	m
l_{tf}	the longitudinal position of the front bogie traction rod connection point with the car body to the car body rear end	21.2	m
l_{tr}	the longitudinal position of the rear bogie traction rod connection point with the car body to the car body rear end	3.3	m
l_{yf}	the longitudinal position of the front bogie yaw damper connection point with the car body to the car body rear end	21.66	m
l_{yr}	the longitudinal position of the rear bogie yaw damper connection point with the car body to the car body rear end	2.84	m
l_w	half distance between the two wheelsets of the bogie	1.25	m
m_b	mass of the bogie frame	2580	kg
m_c	mass of the car body	16900	kg
m_w	mass of the wheelset	1510	kg
N_{wij}	the normal contact force between the jth wheelset of ith bogie frame and the rail	-	N
r_w	wheel radius	0.43	m
v	vehicle velocity	300	km.h^{-1}
ω_{1b}	the first bending mode frequency of the car body	9.84	Hz
ω_{2b}	the second bending mode frequency of the car body	15.12	Hz
$\omega_{1\varphi}$	the first twisting mode frequency of the car body	13.42	Hz
ξ_{1b}	damping coefficient for the first flexible bending mode	0.012	-
ξ_{2b}	damping coefficient for the second flexible bending mode	0.003	-
$\xi_{1\varphi}$	damping coefficient for the first flexible twisting mode	0.011	-